Journal of Cleaner Production 277 (2020) 123830

Contents lists available at ScienceDirect

Journal of Cleaner Production

journal homepage: www.elsevier.com/locate/jclepro

Satellite-based mapping of the Universal Thermal Climate Index over the Yangtze River Delta urban agglomeration

Chenguang Wang [a], Wenfeng Zhan [a, b, *], Zihan Liu [a], Jiufeng Li [a], Long Li [c], Peng Fu [d], Fan Huang [a], Jiameng Lai [a], Jike Chen [e], Falu Hong [a], Sida Jiang [a]

[a] Jiangsu Provincial Key Laboratory of Geographic Information Science and Technology, International Institute for Earth System Science, Nanjing University, Nanjing, 210023, China
[b] Jiangsu Center for Collaborative Innovation in Geographical Information Resource Development and Application, Nanjing, 210023, China
[c] Key Laboratory of Virtual Geographic Environment of Ministry of Education, College of Geographic Science, Nanjing Normal University, Nanjing, 210023, China
[d] Department of Plant Biology, University of Illinois at Urbana-Champaign, Urbana, IL, 61801, USA
[e] School of Remote Sensing and Geomatics Engineering, Nanjing University of Information Science and Technology, Nanjing, 210044, China

ARTICLE INFO

Article history:
Received 26 April 2020
Received in revised form
25 June 2020
Accepted 14 August 2020
Available online 2 September 2020

Handling editor: Cecilia Maria Villas Bôas de Almeida

Keywords:
Universal thermal climate index (UTCI)
Remote sensing
Thermal comfort
Urban heat island
MODIS
Yangtze river delta urban agglomeration

ABSTRACT

The Universal Thermal Climate Index (UTCI) is an important and frequently used indicator for evaluating thermal comfort. However, there is a lack of city-scale UTCI mapping over urban agglomerations during heat waves, and of studies of the variation of UTCI-based urban heat island intensities across cities. In addition, there is a need to evaluate the relationships among UHI intensities calculated by different types of temperature. In this study of the Yangtze River Delta urban agglomeration (YRDUA), we conducted city-scale UTCI mapping during periods of heat waves, based largely on satellite data. We then compared the UHI intensities in three megacities (Nanjing, Shanghai, and Hangzhou) in terms of the UTCI, and distinguished the differences between UHI intensities based on different types of temperature. Our principal findings are as follows: (1) The UTCI varies considerably with land cover type, with values generally higher in urban areas. Although the spatial pattern of UTCI and air temperature appears similar, over urban surfaces the former indicator is significantly higher than the latter. (2) The areas affected by (very) strong thermal stress (quantified by the UTCI) expanded by 18% and 36.2%, respectively, during daytime and nighttime over the YRUDA from 2002 to 2018. The increase occurred mainly in city peripheries where rapid urbanization has occurred. (3) The UTCI-based UHI intensity (UHII) is lower than those based on land surface temperature (LST) and mean radiant temperature, but greater than those based on surface air and dew-point temperature. The difference among these UHIIs (i.e., UTCI- and other temperature-based measures) over the three selected megacities are relatively small in the day, but they are relatively large at night. Our results are potentially valuable for facilitating city-scale UTCI mapping and for evaluating thermal comfort at the regional scale.

1. Introduction

Thermal comfort is a biometeorological indicator based on heat exchange between human bodies and their surroundings (Fanger, 1970), and it has frequently been used to assess the overheating risk of human bodies at different spatiotemporal scales. There is an increasing incidence of heat waves (occurrence of extreme high temperatures) worldwide, mostly due to the aggregation of escalating global warming and urban heat islands (UHIs) (Anderson and Bell, 2010; Barriopedro et al., 2011; He et al., 2020; Meehl and Tebaldi, 2004; Trenberth and Fasullo, 2012; Zuo et al., 2015). These widespread heat waves have drastically altered thermal comfort and exacerbated human health risks, resulting in increased mortality (Anderson and Bell, 2009; Hajat et al., 2010; Mora et al., 2017; Schwartz et al., 2004). There is currently a large impetus to explore the spatiotemporal variations of thermal comfort, especially over urban agglomerations during heat wave events, in order to support the development of adaptation strategies to mitigate

* Corresponding author. Nanjing University at Xianlin Campus, No.163 Xianlin Avenue, Qixia District, Nanjing, Jiangsu, 210023, PR China.
E-mail address: zhanwenfeng@nju.edu.cn (W. Zhan).

https://doi.org/10.1016/j.jclepro.2020.123830
0959-6526/

Nomenclature

Acronyms

ALR	adiabatic lapse rate
ECMWF	European Centre for Medium-Range Weather Forecasts
IGBP	international geosphere-biosphere programme
LST	land surface temperature
MODIS	moderate resolution imaging spectroradiometer
MENEX	Man-ENvironment heat Exchange
NDVI	normalized difference vegetation index
PET	physiologically equivalent temperature
PT	perceived temperature
SD	standard deviation
SET	standard effective temperature
UTCI	universal thermal climate index
UHI	urban heat island
WRF	weather research and forecasting
YRDUA	Yangtze River Delta urban agglomeration

Variables used in equations

g	acceleration of gravity
I_{pixel}	pixel-based UHII
I_{mean}	mean UHII for each city
p_s	pressure at the surface
p_L	bottom pressure
p_{L1}	pressure at the lowest level in the atmospheric profile
p_{L2}	pressure at the level above p_{L1}
T_a	surface air temperature
T_{a_L}	atmospheric temperature corresponding to p_L
T_{a_L1}	atmospheric temperature corresponding to p_{L1}
T_{a_L2}	atmospheric temperature corresponding to p_{L2}
T_d	surface dew-point temperature
T_{d_L1}	dew-point temperature corresponding to p_{L1}
T_{d_L2}	dew-point temperature corresponding to p_{L2}
T_{mrt}	mean radiant temperature
T_s	land surface temperature
T_{rural}	mean temperature for the rural areas
T_{urban}	mean temperature for the urban areas
VP	atmospheric vapor pressure
V_s	wind speed
σ	Stefan-Boltzmann constant
ε_a	air emissivity
ε_g	land surface emissivity
ε_p	emissivity of the human body surface
ε_{sky}	clear-sky emissivity
ρ	air density

heat risks (Lavell et al., 2012; Lai et al., 2019).

In the past few decades, numerous indicators have been designed to quantify thermal comfort based on human heat budget models; they include Physiologically Equivalent Temperature (PET), Perceived Temperature (PT), Standard Effective Temperature (SET), and Universal Thermal Climate Index (UTCI) (Błażejczyk et al., 2013; Gagge et al., 1986; Gonzalez et al., 1974; Mayer and Höppe, 1987; Staiger et al., 2012). Indicators such as the PET, PT, and SET adopt models with only two nodes simplified from thermophysiology and heat exchange theories (Pappenberger et al., 2015), and as a result they are relatively insensitive in complex environments (Fiala et al., 2012). In contrast, the UTCI employs the multi-node model (Psikuta et al., 2012), in which a variety of meteorological variables are incorporated (e.g., air temperature, mean radiant temperature, and wind speed). Compared with the other indicators, the UTCI better considers the surrounding environment, human physiological characteristics, and the thermal resistance of clothing (Błażejczyk et al., 2012; Höppe, 2002). These additional considerations increase its sensitivity to changes in meteorological variables and consequently enhance its suitability for quantifying thermal comfort under various climates. They also make the UTCI more adaptive for describing changes in the thermal environment and therefore it is appropriate for the evaluation of thermal comfort (Jendritzky et al., 2012).

Previous estimations or mapping of the UTCI have been conducted at the site, local (or neighborhood), and continental (or global) scales. At the site scale, the UTCI estimation relies mainly on ground-based measurements of various meteorological variables (e.g., air temperature and mean radiant temperature). Based on such measurements, the spatiotemporal variation of the UTCI and its relationships with associated meteorological variables have been studied at the site scale (Bröde et al., 2012b). Rapid UTCI mapping over a relatively larger area is valuable for applications such as urban planning and the evaluation of health risk induced by heat waves (Chen and Ng, 2011; Jendritzky and Tinz, 2009). However, the limited and sometimes sparsely distributed site-based meteorological stations hinder the use of UTCI mapping for cities with high spatial heterogeneity, which limits our understanding of thermal comfort at a larger spatial scale. At the local (or neighborhood) scale, a variety of approaches have been proposed for mapping UTCI in recent years. One frequently-used approach is to combine ground-based measurements and model simulations (e.g., by the ENVI-Met) (Battista et al., 2016; Park et al., 2014; Tumini et al., 2016; Xu et al., 2019). The recently available LiDAR technology is also useable for supporting UTCI mapping (Chen et al., 2016). These approaches have the advantage of completely accounting for urban geometry and fabrics (Alavipanah et al., 2018; Bröde et al., 2012a,b; Johansson and Emmanuel, 2006; Mijorski et al., 2019). In addition to urban micro-structure and micro-climate, the UTCI is also controlled by a series of environmental factors such as the background climate at an even larger scale (Ho et al., 2016). Nevertheless, UTCI mapping at the local (or neighborhood) scale is unable to fully reflect the influences of such environmental controls at a very large scale (Pappenberger et al., 2015). At the continental (or global) scale, this *status quo* gives rise to the use of reanalysis data to support UTCI mapping, with a spatial resolution of around or coarser than 10 km (Di Napoli et al., 2018; ECMWF, 2020; Pappenberger et al., 2015).

Although advances in UTCI mapping have been achieved at various spatial scales (i.e., the site, local, and continental scales), here we identify a gap at the regional scale (or city-scale) over which inter- and inner-city variations in thermal comfort can be properly balanced, especially from the following three perspectives. First, satellite remote sensing data, usually with a spatial resolution ranging from meters to kilometers, are well suited for supporting UTCI mapping at the regional scale; e.g., satellite-derived land surface temperatures (LSTs) from Landsat have been employed for mapping the UTCI (Błażejczyk, 2011). However, the relatively narrow swath (185 km) and long revisit cycle (16 days) of Landsat data hinder their application at the regional scale during required periods. Second, although thermal comfort can be exacerbated with the superposition of UHIs and heat waves (Arghavani

et al., 2020; Hajat et al., 2010; Imran et al., 2018; Mora et al., 2017), no single study has yet accomplished UTCI mapping over an urban agglomeration during heat waves. Third, the UHI intensity (UHII) is an indicator describing the urban influence on the background thermal environment (Liu et al., 2020; Oke et al., 2017), and it has been quantified by different types of temperature (e.g., skin-surface, surface air, and apparent temperatures) (Ho et al., 2016; Hu and Brunsell, 2015; Imhoff et al., 2010; Voogt and Oke, 2003). However, it remains unclear how the UTCI-based UHII would vary across cities within an urban agglomeration, particularly compared with UHI intensities calculated by other types of temperature.

In view of these challenges, in this study we attempted to conduct UTCI mapping largely with the assistance of satellite data at the city scale, especially over an urban agglomeration during heat wave periods. We also examined the variations of UTCI-based UHI intensities over typical cities in the Yangtze River delta region of China and compared them with those quantified by other types of temperature. We hoped that the results of the study would help advance UTCI mapping and deepen our understanding of the urban thermal environment. The rest of this article is organized as follows: Subsequent to the description of the study area in Section 2, Section 3 presents data and methodology for satellite mapping of UTCI. Results and discussion are presented in Section 4; and the conclusion is finally drawn in Section 5.

2. Study area

The Yangtze River delta urban agglomeration (YRDUA), which contains a total of 16 cities, was selected as the study area (Fig. 1). The YRDUA is located in the lower reaches of the Yangtze River adjacent to the East China Sea. It is one of the three largest urban agglomerations in China with a population of more than 100 million. The terrain is dominated by plains with several mountains and hills in the southwest.

With a subtropical monsoon climate, the region is warm and humid with four distinct seasons. The annual mean temperature range is 18–23 °C, and the highest monthly mean temperature is greater than 28 °C; the annual mean precipitation is 1500 mm. The western Pacific subtropical high pressure zone makes it one of the warmest regions in summer over mainland China, and heat waves are quite common (Gao et al., 2015). In the past several decades, the region has experienced rapid economic development and urbanization, resulting in gradually increasing UHIs across all of the cities (Feng et al., 2012; Yang et al., 2017). The combination of more frequent heat waves and increased UHIs has reduced the thermal comfort and increased the associated health risks within the region (Hu et al., 2017; Kong et al., 2017).

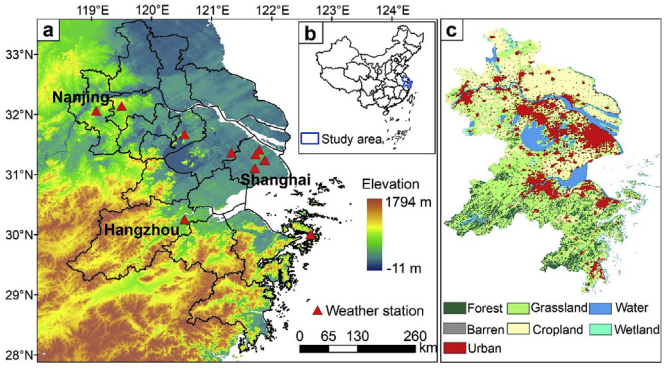

Fig. 1. Geolocation and surface properties across the Yangtze River delta urban agglomeration (YRDUA). Elevation and spatial distribution of the meteorological stations used in this study (**a**), location of the YRDUA in China (**b**), and the land cover types (**c**).

3. Data and methods

3.1. Data

3.1.1. Meteorological data

The meteorological data used in this study include air temperature, dew-point temperature, and wind speed, for the interval from 2002 to 2018. All of these data were obtained from the publicly accessible Weather Underground (https://www.wunderground.com/). Considering that hourly meteorological observations are required to match the overpasses of satellite data, a total of ten stations across the YRDUA were retrieved (see Fig. 1a for the retrieved stations). Notably, the wind speed data were directly used to assist in calculating the UTCI as it is difficult to estimate this parameter using remote sensing. Surface air and dew-point temperatures were used to evaluate the accuracies of the parameters that were retrieved by remote sensing.

3.1.2. Satellite data

We used five satellite products acquired by Moderate Resolution Imaging Spectroradiometer (MODIS) (onboard the Aqua satellite) for 2002–2018, including the LST (MYD11_L2, daily), Atmosphere Profile (MYD07_L2, daily), Cloud Mask (MYD35, daily), Normalized Difference Vegetation Index (NDVI) (MOD13A2, 16-day composites), and yearly land cover type (MCD12Q1) data. The Aqua rather than the Terra satellite was chosen because the transit time of Aqua in the afternoon (at ~13:30 local solar time) corresponds better to the daily maximum temperature during summer. All of these data were downloaded from the EOSDIS (https://search.earthdata.nasa.gov/search). Detailed information on these MODIS products is given in Table 1.

The LST product (i.e., MYD11_L2) was used to obtain the LST and to estimate the mean radiant temperature. The atmospheric profiles product (i.e., MYD07_L2) was used to estimate or retrieve the surface air and dew-point temperatures. The cloud mask product (i.e., MYD35) was used to detect clear-sky pixels (or the cloud percentage in contrast) and to estimate the solar radiation flux, facilitated by the already-calculated mean radiant temperature. The NDVI data retrieved from MYD13A2 were used to investigate the relationship between UTCI and vegetation coverage. The main land cover types retrieved from MCD12Q1 include bare soil, water, forest, grassland, farmland, towns, and wetlands across the YRDUA (Fig. 1c).

Data pre-processing steps such as geometric correction, image mosaicing, and resampling were performed on the raw images. The MODIS Reprojection Tool was directly used for the image mosaicing of the LST, cloud mask, and NDVI data, while the MODIS Conversion Toolkit was used for processing atmospheric profile data. Note that all the MODIS data were resampled to the same resolution (i.e., 1 km).

3.2. Methods

A heat wave period was defined as the scenario in which the daily maximum temperature exceeded 35 °C for three consecutive days (Gao et al., 2015; Huang et al., 2010; Sun et al., 2014). To avoid data gaps due to clouds, the LST data during the heat wave period were composited to obtain spatially continuous UTCIs (Di Napoli et al., 2018; Yang et al., 2018).

A flowchart for the satellite-based UTCI mapping is presented in Fig. 2. The UTCI involves four parameters as inputs: surface air temperature (T_a), atmospheric vapor pressure (VP), mean radiant

Table 1
Detailed information on the MODIS products used in this study.

Product name	Product type	Resolution (km)	Temporal granularity
MYD11_L2	Land Surface Temperature & Emissivity	1	Daily
MYD07_L2	Atmosphere Profile Product	5	Daily
MYD35	Cloud Mask and Spectral Test Results	1	Daily
MYD13A2	Vegetation Indices	1	16-Day
MCD12Q1	Land Cover Type	0.5	Yearly

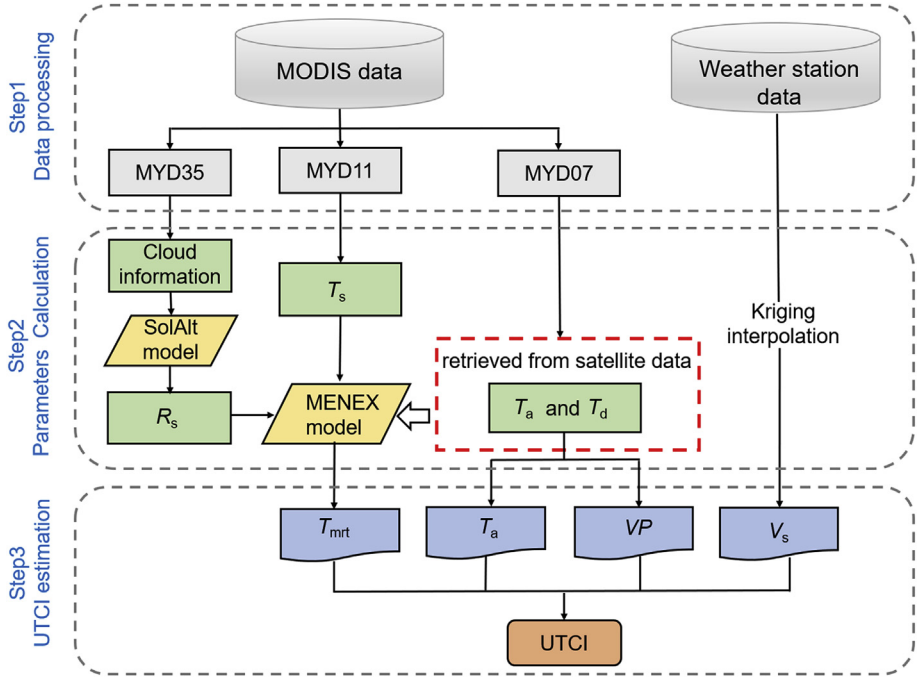

Fig. 2. Flowchart of the satellite mapping of the UTCI (the parameters in the blue boxes are required for calculating UTCI). T_s, T_a, T_d, and T_{mrt} represent the land surface temperature, surface air temperature, dew-point temperature, and mean radiant temperature, respectively; and R_s, VP, and V_s are the shortwave solar radiation, atmospheric vapor pressure, and wind speed, respectively. The SolAlt and MENEX models were used to help estimate T_{mrt} (further explanation is given in Section 3.2.3). (For interpretation of the references to colour in this figure legend, the reader is referred to the Web version of this article.)

temperature (T_{mrt}), and wind speed (V_s) (Jendritzky et al., 2012). All of these parameters can be estimated from remote sensing data, except V_s. In detail, T_a was directly retrieved from the MYD07_L2 product (Bisht and Bras, 2010) (see Section 3.2.3). *VP* was indirectly estimated based on the surface dew-point temperature (T_d), which was retrieved in a similar way to T_a (Section 3.2.2). The calculation of T_{mrt} is relatively complex because human bodies can receive radiation from various directions. Here we mainly considered the impacts of solar shortwave radiation and surface emitted longwave radiation, quantified by the Man-ENvironment heat Exchange (MENEX) model that requires the T_s, T_a, *VP*, and the cloud mask as inputs (Section 3.2.3). V_s was interpolated from ground-based measurements (Section 3.2.4). Finally, we estimated UTCI based on an established look-up table between UTCI and the aforementioned parameters (Bröde et al., 2012b).

3.2.1. Estimation of instantaneous T_a

T_a is one of the most basic parameters for calculating the UTCI. T_a can be measured directly with ground-based instruments, but such *in-situ* measurements cannot accurately capture the thermal status at a large scale, especially over urban surfaces that are characterized by high heterogeneity (Ho et al., 2014; Xu et al., 2014). Satellite data can overcome the inaccurate proxy of ground-based measurements through pixel-based sampling. Here we used the atmospheric profile product (MYD07_L2) to estimate T_a because of its demonstrated high accuracy in various applications (Jang et al., 2010; Hu and Brunsell, 2015).

Each profile within the MYD07_L2 product is divided into 20 layers depending on pressure. According to the hydrostatic assumption, T_a can be retrieved by the adiabatic lapse rate (ALR) using a simple parameterization method (Bisht and Bras, 2010; Zhu et al., 2017), given as:

$$T_a = T_{a\_L} - \mathrm{ALR}/\rho g \cdot (p_s - p_L) \quad (1)$$

where T_a is the air temperature at the surface; T_{a_L} is the atmospheric temperature at the lowest pressure level in the atmospheric profile; p_s and p_L are the pressure at the surface and the bottom pressure, respectively; and ρ and g are two constants which denote the air density and acceleration of gravity, respectively. For Eq. (1), the air temperatures and pressure are available in the atmospheric profiles, and therefore T_a can be estimated by the ALR, which is calculated using the two pressure levels closest to the surface (Zhu et al., 2017). Consequently, T_a can be estimated by reformulating Eq. (1), as follows:

$$T_a = T_{a\_L1} - \left[\left(T_{a\_L2} - T_{a\_L1}\right) / \left(p_{L2} - p_{L1}\right)\right] \cdot (p_s - p_{L1}) \quad (2)$$

where p_{L1} is the pressure at the lowest level in the atmospheric profile; p_{L2} is the pressure level above p_{L1}; and T_{a_L1} and T_{a_L2} are the

atmospheric temperatures retrieved at the two pressure levels p_{L1} and p_{L2}, respectively. The estimated T_a was validated with *in-situ* measurements and showed a satisfactory degree of accuracy. More details on the validation are given in the Appendix.

3.2.2. Estimation of instantaneous T_d

Similar to T_a, the near-surface T_d can be retrieved from the multi-layer dew-point temperature data provided by the MYD07_L2 product (Jang et al., 2010; Zhu et al., 2017), which is expressed as follows:

$$T_d = T_{d\_L1} - \left[\left(T_{d\_L2} - T_{d\_L1}\right) / \left(p_{L2} - p_{L1}\right)\right] \cdot \left(p_s - p_{L1}\right) \quad (3)$$

where T_d is the surface dew-point temperature, and the other parameters are similar to those given in Eq. (2). Note that the UTCI requires *VP* rather than T_d as the input. *VP* (hPa) and T_d are convertible using the following formula (Bolton, 1980):

$$VP = 6.112 \cdot \exp[5417.753 \cdot ((1/273.15) - (1/(273.15 + T_d)))] \quad (4)$$

3.2.3. Estimation of Tmrt

T_{mrt} determines a large proportion of the energy balance of human bodies and therefore the thermal comfort (Clark and Edholm, 1985; Winslow et al., 1936). T_{mrt} represents all of the shortwave and longwave radiation from various surfaces (Fanger, 1970). Since it is difficult to quantify the radiation from each direction directly to estimate T_{mrt} at the satellite scale, here we resorted to the MENEX model (Błażejczyk, 2001, 2007; Błażejczyk and Matzarakis, 2007; Matzarakis et al., 2010), in which T_{mrt} can be estimated with the following equation:

$$T_{mrt} = \left[\left(R_s + L\right) / \left(\varepsilon_p \cdot \sigma\right)\right]^{0.25} - 273.15 \quad (5)$$

where R_s and L denote the shortwave and longwave radiation absorbed by the human body, respectively; ε_p is the emissivity of the human body surface set as a constant (0.97); and σ is the Stefan-Boltzmann constant. R_s can be calculated using one of three models: SolDir, SolGlob, and SolAlt (Błażejczyk, 2001). We selected SolAlt to estimate R_s because radiation associated information in the SolDir and SolGlob models is not easily accessible, while only the cloud information, which can be provided by the MYD35 cloud mask product, is required for the SolAlt model. The longwave radiation *L* received by human bodies can be divided into two parts: the ground-emitted radiation (L_g) and the atmosphere-emitted radiation (L_a), which can be calculated by the following (Błażejczyk and Matzarakis, 2007):

$$L = 0.5 \cdot \varepsilon_p \cdot \left(L_a + L_g\right) \quad (6)$$

$$L_a = \varepsilon_{sky} \cdot \sigma \cdot \left(T_a + 273.15\right)^4 \quad (7)$$

$$L_g = \varepsilon_g \cdot \sigma \cdot \left(T_s + 273.15\right)^4 \quad (8)$$

where ε_g is the surface emissivity, and ε_{sky} is the sky emissivity that can be calculated as (Kenny et al., 2008):

$$\varepsilon_{sky} = \varepsilon_a \cdot \left(0.82 - 0.25 \cdot 10^{-0.094 \cdot VP}\right) \quad (9)$$

where ε_a is the emissivity of the air set as 0.97 (Park and Tuller, 2011). *VP* can be obtained from T_d using Eq. (4). Here one could argue that the estimation of T_{mrt} disregards the elaborate urban structure (geometry) that can affect the radiation load. However, it should be noted that (1) this study is focused on the regional scale, and (2) such information on urban structure is actually contained within the remotely sensed T_s (with the resolution of 1 km). Further discussion of this issue is given in Section 4.3.1.

3.2.4. Estimation of V_s

The V_s for each pixel was interpolated based on the measurements obtained at ground-based stations with the Kriging technique implemented with ArcGIS. The Kriging technique has been recommended for the spatial interpolation of variables related to thermal comfort mapping (Błażejczyk et al., 2014; Roshan et al., 2019). We acknowledge that the interpolated V_s may be different from the true values in cities due to the complex urban geometry. Nevertheless we still used the interpolated values because (1) it is difficult estimate the true pixel-based V_s of extensive areas such as an urban agglomeration; (2) the V_s during heat wave periods is usually small (Li and Bou-Zeid, 2013); and (3) the calculation of UTCI is relatively insensitive to V_s (Bröde et al., 2012b; Pantavou et al., 2013). Further discussion of this issue is given in Section 4.3.2.

3.2.5. Calculation of UTCI

With the estimation of the aforementioned parameters, the UTCI can be directly calculated using a look-up table, given as (Bröde et al., 2012b):

$$UTCI = f\left(T_a,\ V_s,\ VP,\ T_{mrt} - T_a\right) + T_a \quad (10)$$

According to the magnitude of thermal stress, the calculated UTCI values can be divided into five categories (Table 2), from which the physiological response of human thermal comfort can be assessed (Bröde et al., 2012b; Jendritzky et al., 2012).

To show typical UTCI maps for the YRDUA during heat wave periods, we chose the summer of 2018 as the major study period for mapping as there were the greatest number of days (i.e., 15 days) with the daily maximum temperature exceeding 35 °C. To obtain gap-free maps, remote sensing data during these 15 days were composited. To illustrate the trajectories in thermal comfort from 2002 to 2018, we further constructed mean UTCI maps during heat wave periods for three different intervals: 2002–2004, 2009–2011, and 2016–2018.

3.3. Calculation of UHII

The UHII can be computed using different types of temperature. Here we calculated the UHIIs quantified by T_s (surface UHI), T_a (canopy UHI), T_d, T_{mrt}, and UTCI. Three typical cities (Nanjing, Shanghai, and Hangzhou) with a large urban size and population were selected to compare UHIIs with different types of temperature.

Delineation of the urban area and the associated rural background was required for UHII calculation. The extent of the urban area was determined according to the land cover type product (MCD12Q1), while the rural background was designated as a buffer (with a distance of 15 km) surrounding the urban area boundary

Table 2
Equivalent temperatures of the UTCI categorized in terms of thermal stress.

UTCI range (°C)	Stress category	Number
above +46.0	Extreme heat stress	4
+38.1 to +46.0	Very strong heat stress	3
+32.1 to 38.0	Strong heat stress	2
+26.1 to +32.0	Moderate heat stress	1
+9.1 to 26.0	No thermal stress	0

(Bechtel, 2015; Clinton and Gong, 2013). Based on this delineation, the mean UHII for each city (I_{mean}) and the pixel-based UHII (I_{pixel}) were calculated as follows:

$$\begin{cases} I_{mean} = T_{urban} - T_{rural} \\ I_{pixel} = T_{pixel} - T_{rural} \end{cases} \quad (11)$$

where T_{urban} and T_{rural} are the mean temperature for urban and rural areas, respectively; and T_{pixel} is the temperature of each pixel within the city.

4. Results and discussion

4.1. Assessment of spatiotemporal patterns in UTCI

4.1.1. Assessment of spatial patterns in UTCI

The spatial patterns in daytime and nighttime UTCI across the YRDUA during the heat wave periods in 2018 are presented in Fig. 3. The UTCI tends to be higher within and around urban areas, and it is also generally higher in the mountains and lower in the plains. During the day, the UTCI shows a large degree of spatial variation, with the difference between maximum and minimum values of 13.7 °C. By comparison, the nighttime UTCI variability is relatively small, especially in the plain areas. The results also reveal that UTCI values tend to be lower in the coastal areas at night. To better assess the spatial patterns in UTCI, the following two subsections focus on the UTCI variations, in light of the different land cover types and variety of temperatures.

The spatial patterns in UTCI are closely related to local surface properties such as terrain and land cover type (Fig. 3). The spatial variations in UTCI are relatively more impacted by land cover type than by terrain, as the YRDUA is mainly located in plains where the terrain is relatively flat. To better examine the relationship between UTCI and land cover type, the UTCI values for each land cover type were calculated and compared (Fig. 4).

The results show a large degree of variation in UTCI over different land cover types during the daytime. Among these types, the urban surfaces that are characterized by high density buildings and low vegetation coverage have the highest UTCI. The higher UTCI over urban surfaces can be attributed to their underlying impervious surfaces that generally exhibit significantly higher T_{mrt} and T_a (Benali et al., 2012; Thorsson et al., 2014). However, the

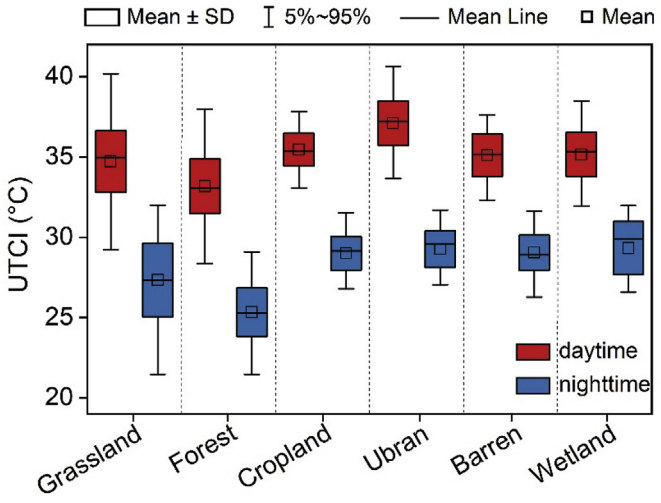

Fig. 4. Boxplots of the daytime and nighttime UTCI values over different land cover types.

reasons why forest and grassland correspond to higher UTCI values can be attributed to two important factors. First, the evapotranspiration over vegetation and the sheltering effect of the canopy can effectively reduce T_s, which can lead to a decrease in T_{mrt} and T_a and consequently to a reduction in UTCI. Second, most of the forests and grasslands are located in mountainous areas with high altitudes where T_d is often lower, which can also lead to a decreased UTCI (Prihodko and Goward, 1997; Zakšek and Schroedter-Homscheidt, 2009). The UTCI difference between urban land and forest can be up to 3.93 °C during the daytime. Strong solar insolation during the day and the difference in heating rates over these two land cover types may cause this large contrast. The UTCI values of other land surface types (mostly natural surfaces located in the plains) have a smaller degree of spatial variation, which is generally intermediate between those over urban surfaces and forests.

The UTCI is generally lower during nighttime compared to daytime, and the spatial variations in nighttime UTCI among different land cover types are similar to those in daytime UTCI (Fig. 4). However, compared with the daytime UTCI, there are two main deviations at night. First, the contrast among different land

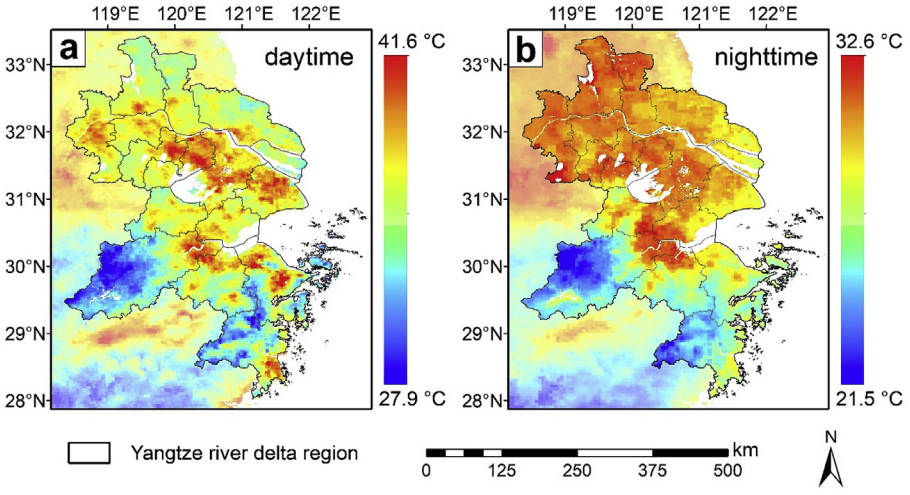

Fig. 3. Spatial distribution of UTCI during daytime (**a**) and nighttime (**b**) in the Yangtze River Delta urban agglomeration in the summer of 2018.

(1) Relationships between UTCI and different land cover types

cover types is relatively small (less than 0.5 °C); e.g., the difference in UTCI between urban surfaces and other land cover types is much smaller at night than during the day, due mainly to the significantly reduced nighttime T_s over urban areas compared to that during the day. Second, the mean UTCI reaches the highest values in wetlands at night. This may be due to the suppressed cooling process in wetlands, caused by the larger specific heat capacity of water.

To better assess the spatial patterns in UTCI within urban areas, the relationships between UTCI and NDVI were further investigated via a feature space formulated using these two parameters as the x- and y-coordinates, respectively (Fig. 5). The results show that the distributions of the points are generally triangular- or trapezoidal-shaped within the feature space. During the day, the points are much more scattered than those at night when clusters in areas with higher UTCIs are observed (Fig. 5b). For both daytime and nighttime, a small NDVI value usually corresponds to a high UTCI value, while the UTCI value has a high degree of variation – it can either be high or relatively low when the NDVI value is high (Fig. 5). The former phenomenon is anticipated because low vegetation cover (i.e., with high fraction of impervious surface) often results in low thermal comfort in urban areas, while the latter phenomenon more interestingly indicates that the thermal comfort in urban areas would not be improved by simply increasing the vegetation coverage. There may be three explanations for this. First, while the increase in NDVI may truly reduce T_s and T_a, it may also increase T_d (related to relative humidity) and therefore cause a larger variation in UTCI variation. Second, the NDVI alone is unable to fully characterize the complex surfaces of an urban area, and it is therefore unable to fully capture the variations in UTCI. Third, a high NDVI value may correspond to either dense grassland or forest, over which the UTCI variation can be large.

To examine the impacts of different meteorological variables on the UTCI, the UTCI was compared with several other types of temperature measurement. The UTCI is mainly determined by T_a, T_d, and T_{mrt}, and it is also indirectly affected by T_s that is closely related to T_a and T_{mrt}. The comparison of the spatial patterns, in terms of types of temperature measurement, is shown in Fig. 6. Despite the general similarities of their patterns, differences also exist. T_s possesses the highest spatial heterogeneity – the standard deviation (SD) of T_s is 2.9 °C (1.6 °C) for the day (at night). The variability in T_a is relatively smaller and similar to that of the UTCI. The spatial patterns in T_d contrast the most with the UTCI: higher T_d values appear mainly around lakes and coastal areas, affected by the high humidity of these surrounding water bodies. The spatial pattern of T_{mrt} is similar to that of T_s during the day, while it is closer to that of T_a at night.

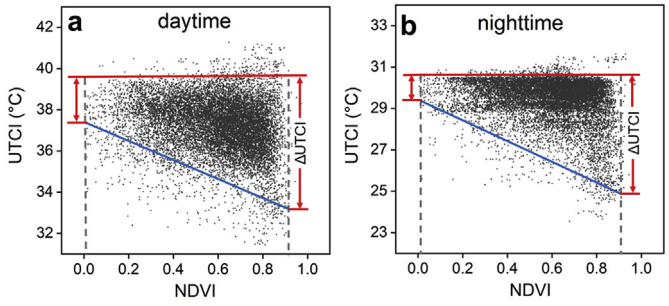

Fig. 5. Relationships between the UTCI and NDVI for urban surfaces during daytime (**a**) and nighttime (**b**) across the YRDUA. The two gray dashed lines contain the range of the NDVI values; and the red and blue lines respectively represent the upper and lower boundaries of the shape formulated by the data points, each denoting an urban pixel with a specific NDVI and UTCI value. (For interpretation of the references to colour in this figure legend, the reader is referred to the Web version of this article.)

(2) Comparison of the UTCI with other types of temperature

Although the general spatial patterns of T_a are similar to those of the UTCI (Fig. 6), there are several significant differences (Fig. 7). The comparison shows that the maximum difference between these two temperatures during the daytime can reach 8.6 °C (Fig. 7a). The higher differences in UTCI and T_a primarily appear in urban and coastal areas, while the differences are quite small in cropland and high-altitude mountainous areas. Specifically, within the urban areas of cities such as Shanghai, Hangzhou, Nanjing, Suzhou, and Wuxi, the UTCI is significantly higher than T_a. At night, the UTCI is closer to T_a. However, there are large differences between UTCI and T_a around water bodies, because of the relatively high T_d at night. In addition, the differences between the UTCI and T_a are much higher around Hangzhou Bay, and further examples of this phenomenon are given in Section 4.2.

Reference to Fig. 6 shows that the UTCI values are generally higher in urban areas than for other surfaces, and this phenomenon can be also observed with respect to the other types of temperature. Considering the generally lower thermal comfort (higher temperatures) within cities, we therefore analyzed the relationships between the UTCI and the other types of temperatures over urban areas in particular (Fig. 8). In general, the correlation between the UTCI and other temperatures is lower during the day than at night. The correlation between the UTCI and T_a is the strongest, with the nighttime R^2 of 0.92, indicating that the UTCI is determined to a high degree by T_a at night. Although T_{mrt} is also strongly correlated with the UTCI, T_{mrt} is significantly lower than its counterpart. This is because in calculating T_{mrt}, the human body is represented as a vertical cylinder, which only receives half of the surrounding radiation (i.e., any point on the cylinder only 'sees' half of the ground and sky and hemisphere) (Kenny et al., 2008). Because of the strong spatial heterogeneity of T_s, the UTCI is less strongly correlated with T_s, especially during the day when the R^2 is only 0.11. Compared with other types of temperature, UTCI has the lowest correlation with T_d, with an R^2 of 0.06 and 0.07 for daytime and nighttime, respectively. One possible explanation may be that the UTCI is a combined indicator that reflects the status of both the surface and the atmosphere, while T_d only reflects the status of the atmosphere. Another factor which may contribute to this weaker correlation is that the UTCI was not calculated directly from T_d, but by *VP* which is converted from T_d.

4.1.2. Assessment of temporal changes in UTCI

The temporal changes in UTCI during the heat wave periods during three stages (i.e., 2002–2004, 2009–2011 and 2016–2018) are illustrated in Fig. 9. The results show that the areas with high UTCI values have expanded gradually during the past two decades, especially in densely populated regions such as Suzhou, Wuxi, and Hangzhou Bay. During the day, the areas with increased UTCI values are generally consistent with those that experienced urban expansion. At night, the areas with significantly increased UTCI values are larger, i.e., not confined to urban areas but extending into the plains with no urban expansion. The change in UTCI at night generally follows an increasing trend from coastal to inland areas, probably as a result of the effect of proximity to the ocean. Furthermore, there is a significant increase in UTCI around Hangzhou Bay at night.

Based on the UTCI values during the three stages, the heat stress was evaluated and classified (Fig. 10). Over these past years, the YRDUA has experienced a continuous expansion of areas classified as 'very strong heat stress', especially over urban or surrounding areas; and the increase in heat stress is relatively more significant from the first (2002–2004) to the second stage (2009–2011) than from the second to the third stage (2016–2018). During the day, the heat stress largely changes from 'strong' to 'very strong' (see

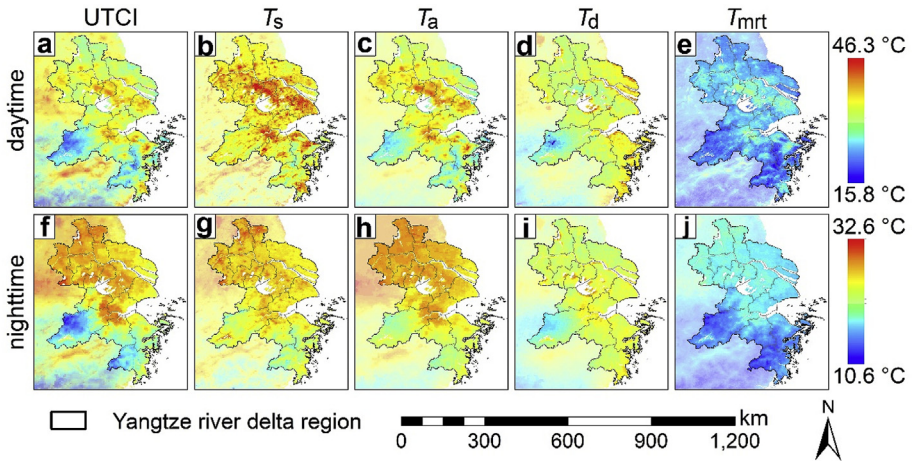

Fig. 6. Comparison of the spatial patterns in UTCI, T_s, T_a, T_d, and T_{mrt} during daytime and nighttime across the YRDUA in the summer of 2018.

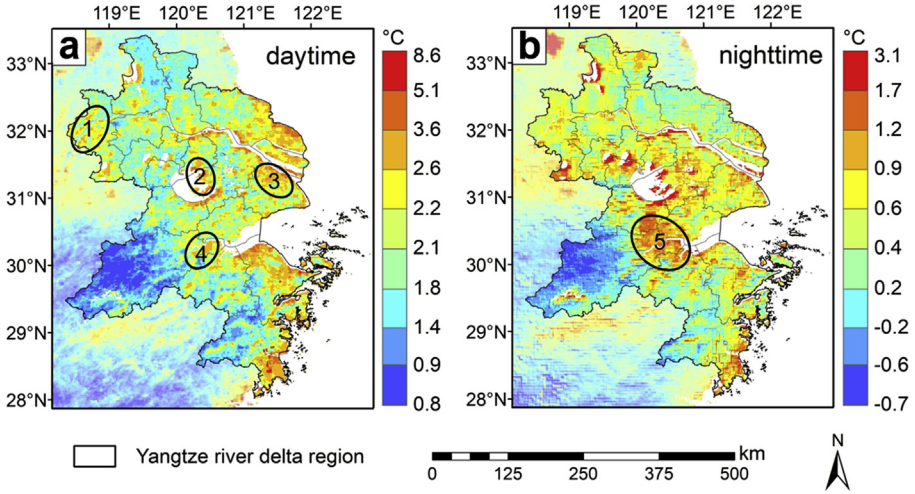

Fig. 7. Spatial distribution of the difference between the UTCI and T_a during heat wave periods in the summer of 2018. Areas with a large difference between the UTCI and T_a are highlighted by an ellipse: Nanjing (Ellipse 1), Suzhou and Wuxi (Ellipse 2), Shanghai (Ellipse 3) and Hangzhou (Ellipse 4), and Hangzhou Bay area (Ellipse 5).

Table 2), especially for those regions around cities. Only a small proportion of the regions (mainly mountainous regions) were affected by moderate heat stress. The temporal variation of heat stress was more significant at night, and the areas affected by strong heat stress have been constantly expanding during the studied interval – the percentage of areas with 'strong heat stress' has changed from the minimum to the maximum.

4.2. Estimation of UHII based on UTCI

Our previous analysis has shown that increased UTCIs mainly occur within or around urban clusters and that they accord well with areas of urban expansion. To further analyze the urbanization impacts on the UTCI, we calculated the UTCI-based UHII and investigated its spatial patterns (Section 4.2.1), and compared them with the UHIs calculated based on other temperatures, i.e., T_s, T_a, T_{mrt}, and T_d (Section 4.2.2).

4.2.1. Spatial patterns of UTCI-based UHI

The UTCI-based UHIIs of three typical cities (Nanjing, Shanghai, and Hangzhou) during the heat waves in 2018 are shown in Fig. 11. During the day, the averaged UHIIs of these three cities show a small difference, with values of 1.07, 1.05, and 1.15 °C for Shanghai, Nanjing, and Hangzhou, respectively. However, the pixel-based variations in UHII are large within each city; for example, the SD of UHII in Shanghai is up to 1.19 °C. This is mainly due to the high degree of heterogeneity of the internal urban structure (or composition) across Shanghai. For Shanghai, the UHII is usually higher in the center and northwest of the city, while it is relatively low in Chongming Island in the northeast and in the riverside areas. For Nanjing, the higher UHII values mainly appear in the southern areas with a higher level of urbanization. The spatial distribution of UTCI-based UHII in Hangzhou differs slightly from those of the other two cities – the higher UHII values are concentrated not only within the city center but also in the southeastern city periphery where the urbanization rate is also high due to the combined impacts of Hangzhou and its neighboring city of Shaoxing.

At night, the UTCI-based UHII varies greatly among the three cities. For Nanjing, the SD of the UHII within the urban boundary is relatively low (0.23 °C at most). For Shanghai, a weak UHII appears in the southeast, likely reflecting the sea breeze effect from the East China Sea. Relatively high UHII values occur in the inland northwest, which is adjacent to areas with a high level of urbanization. For Hangzhou (also a coastal city), the SD of the UHII is smaller than that in Shanghai. This is probably because of the 'wall effect' created

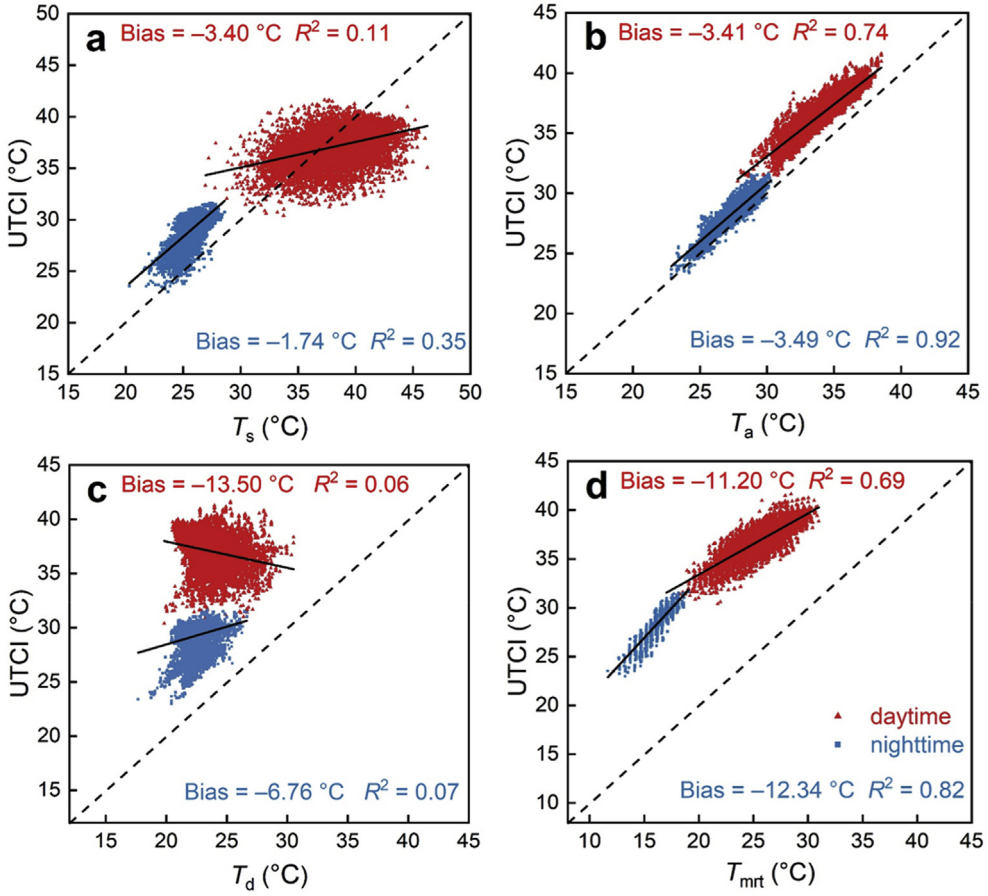

Fig. 8. Relationships between the UTCI and the other types of temperature in urban areas. (**a**), (**b**), (**c**), and (**d**) show the correlation of UTCI with T_s, T_a, T_d, and T_{mrt}, respectively.

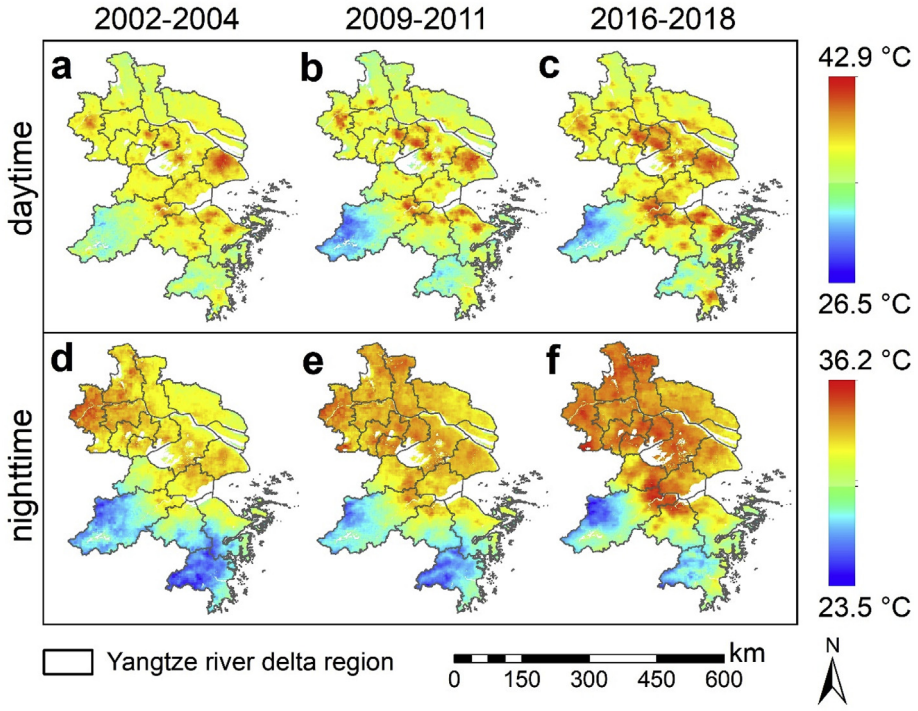

Fig. 9. Temporal changes in UTCI across the YRDUA during three stages of heat wave periods (2002–2004, 2009–2011, and 2016–2018).

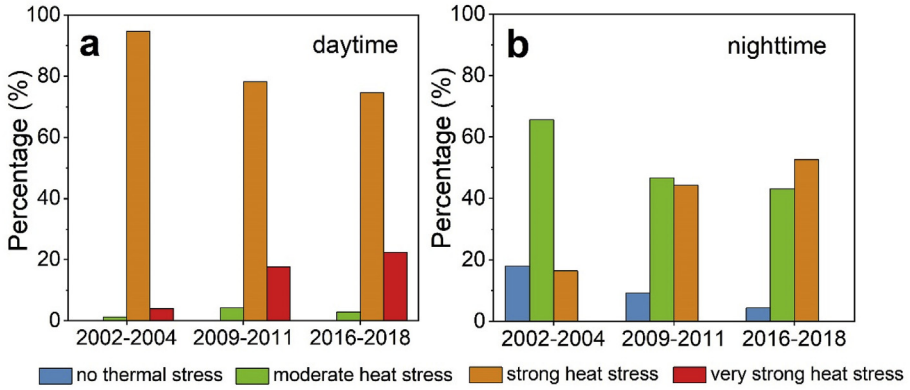

Fig. 10. Temporal changes among different magnitudes of heat stress quantified by the UTCI across the YRDUA during the three stages (2002–2004, 2009–2011, and 2016–2018) during daytime (**a**) and nighttime (**b**).

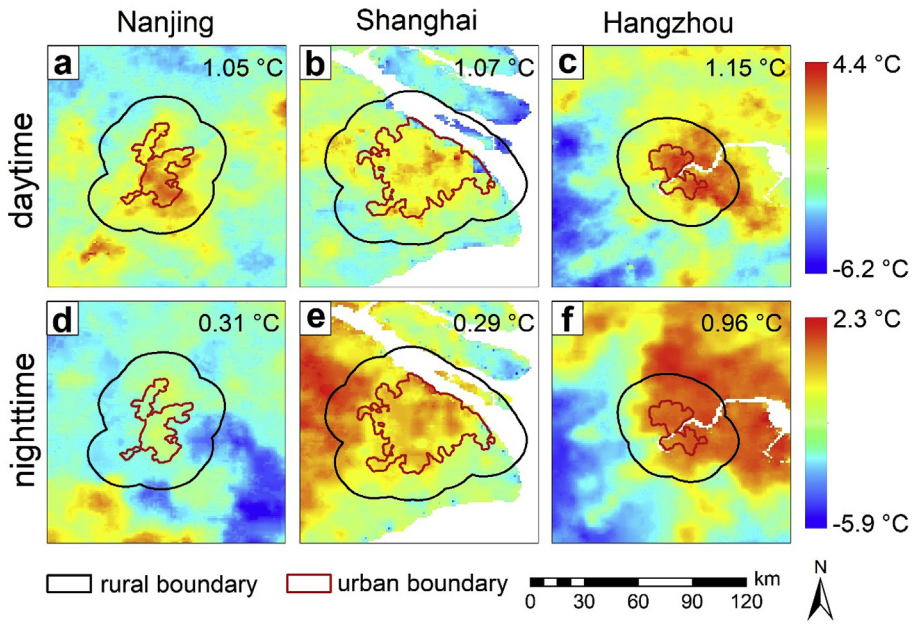

Fig. 11. Spatial patterns of UTCI-based UHII in three typical cities. The mean UHII for each city is shown in the upper right corner of each subfigure.

by the mountains that surround Hangzhou in three directions, which is capable of slowing down the rate of air circulation (sea breeze) and accordingly reduce the spatial difference in UHII (Wong et al., 2011).

4.2.2. Comparison of UHII based on different temperatures

A comparison of the UHII values calculated based on the UTCI, T_s, T_a, T_{mrt}, and T_d is shown in Fig. 12. During the day, the order of the UHII values based on different temperatures is similar for all three cities. The values of UHII are the highest when using T_s, followed by T_{mrt}, UTCI, T_a, and then T_d. The differences among these UHIIs based on different temperatures (e.g., T_s-minus T_d-based UHII) can be up to 3.15, 2.75, and 2.54 °C in Hangzhou, Nanjing, and Shanghai, respectively. The smallest difference among these five types of UHII appears between the UTCI- and T_a-based UHIIs, supported by the similarities of these two types of temperature (further explanation is given in Section 4.1.2).

The nighttime UHIIs based on the five temperatures, by comparison, show a large variation between cities. In Nanjing, the order of UHIIs based on different temperatures is the same as that in daytime: i.e., T_s, T_{mrt}, UTCI, T_a, and T_d decrease in order. The general trend in UHII with different types of temperature in Shanghai is close to that of Nanjing, except that the T_d-based UHII in Shanghai is higher than the T_a-based temperature. The high T_d values in eastern Shanghai, due to the influence of ocean water vapor, probably contribute to the higher T_d-based UHII. In Hangzhou, the T_s-based UHII is 0.87 °C, close to that of Nanjing. However, the UHIIs calculated by other temperatures are significantly higher than those of Nanjing (and Shanghai) – the UTCI-based UHII reaches the highest for Hangzhou. There are three possible reasons for this finding. First, the nighttime decrease in UTCI in the western mountains of Hangzhou is greater than for the other land cover types, causing a significant decrease in the mean UTCI of the suburbs and consequently a high UTCI-based UHII. Second, Hangzhou is surrounded by mountains in three directions, which produces a 'wall effect' that can reduce air circulation and consequently decrease nighttime cooling within the city. Third, due to the influence of water vapor in the Hangzhou Bay area, T_d is often higher and UTCI is sensitive to water vapor, which in turn induces a higher UTCI and therefore leads to a higher UTCI-based UHII.

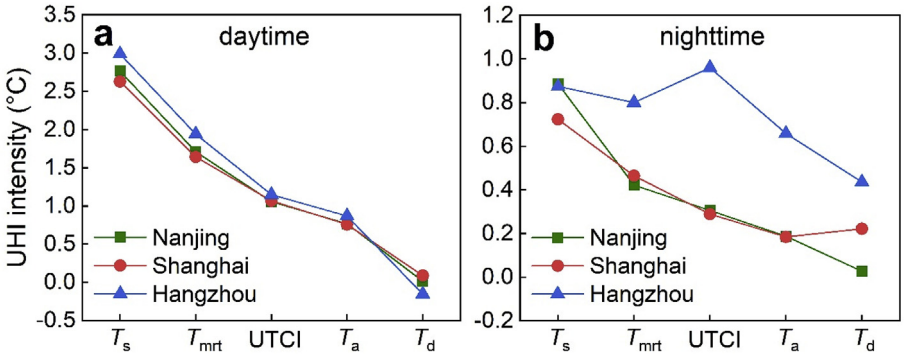

Fig. 12. Comparison of UHIIs based on different types of temperature during heat waves in the summer of 2018 over three typical cities (Nanjing, Shanghai, and Hangzhou) during daytime (**a**) and nighttime (**b**).

4.3. Discussion

4.3.1. Research significance

We have conducted UTCI mapping across an urban agglomeration during heat wave periods, based mainly on satellite data. We further analyzed the UTCI-based UHII and compared it with those calculated based on other types of temperature. Unlike previous studies of the UTCI (Benali et al., 2012; Park et al., 2014), we have mapped the UTCI at a scale that balances spatial resolution and extent: the spatial resolution is sufficiently fine to reveal details of inner-city areas, while the spatial extent is sufficiently large to include an urban agglomeration (inter-city variations). In particular, the UTCI was mapped to provide the thermal comfort status under extreme heat stress.

Previous studies have focused primarily on analyzing either the impacts of the internal urban structure on UTCI at a local scale (Battista et al., 2016; Park et al., 2014; Potchter et al., 2018; Tumini et al., 2016), or on the impacts of the background climate on UTCI at a continental or global scale (Di Napoli et al., 2018; ECMWF, 2020; Pappenberger et al., 2015). However, very few studies have conducted city-scale mapping of UTCI using remote sensing observations with high spatial resolution (Błażejczyk, 2011). One possible reason is the difficulty in obtaining high-accuracy meteorological variables such as T_a and T_d through remote sensing. Although T_s retrieved from Landsat data was used previously in calculating the UTCI (Błażejczyk, 2011), remotely sensed T_s played only a subordinate role in mapping, while most of the parameters required for calculating the UTCI were still obtained from *in-situ* measurements or modelling. To the best of our knowledge, this is the first study to conduct UTCI mapping mainly by satellite remote sensing. In addition, the proposed mapping method is easily applicable over other cities or urban agglomerations, as it is mainly driven by satellite remote sensing data that are publicly available online. The associated city-scale UTCI mapping results, by balancing the inner-city details and inter-city variations, are also potentially useful in a variety of applications such as tourism consulting, urban planning, and health risk assessments (Ge et al., 2017; Jendritzky and Tinz, 2009; Park et al., 2014).

In addition to the studies that focused principally on surface UHIs (denoted by T_s) (Imhoff et al., 2010; Liu et al., 2020; Voogt and Oke, 2003), canopy UHIs (denoted by T_a) (Hu and Brunsell, 2015) or Humidex-based UHIs (Ho et al., 2016), we have further provided UHIs denoted by T_{mrt}, T_d, and finally the UTCI. We analyzed and compared the city- and pixel-based UHI intensities calculated by various types of temperature and summarized their similarities and differences, especially over highly urbanized surfaces. Compared with the other types of temperature, the UTCI is more closely related to heat-induced mortality (Di Napoli et al., 2018; Lokys et al., 2018; Nastos and Matzarakis, 2012), and therefore, the UTCI-based UHIs may also be useful for evaluating heat-related risks.

4.3.2. Sensitivity analysis of the input data used for UTCI mapping

Uncertainties of the input parameters can be propagated into the estimation of UCTI. The approach for retrieving T_s, T_a, T_d, and T_{mrt} using remote sensing is reliable, as is evidenced by previous studies (Chen et al., 2016; Famiglietti et al., 2018; Li et al., 2013; Zhu et al., 2017), and the associated uncertainties for these three parameters are therefore relatively small. It can be argued that T_{mrt} is impacted substantially by urban geometry, which is seemingly absent from the analysis conducted in the present study. Notably, however, T_s used to calculate T_{mrt} already reflects the mean surface thermal status at a scale of 1 km^2 (with a spatial resolution of 1 km), indicating that the 1-km T_s has already incorporated the information on urban geometry. From this perspective, T_{mrt} has included the effects of urban geometry at the spatial resolution of 1 km rather than at the point scale. The interpolation used for obtaining wind speed (V_s) may be less accurate, especially over heterogeneous urban surfaces, and may consequently lead to uncertainties in estimating UTCI. We therefore conducted an additional sensitivity analysis of V_s for the UTCI estimation.

Considering that the error of V_s with Kriging interpolation is usually less than 3 m/s (Apaydin et al., 2004; Luo et al., 2008), we gradually added the errors from 0.5 to 3.0 m/s to the interpolated V_s, with T_a increasing from 20 to 40 °C (with T_{mrt} set equal to T_a and the relative humidity RH set to 50.0% for simplicity) (Fiala et al., 2012), in order to test the sensitivity of interpolation errors to the estimated UTCI (Fig. 13). The results show that the impact of the uncertainty in V_s decreases with increasing T_a. For example, an additional error of 0.5 m/s in V_s will lead to a deviation of 0.5 °C in UTCI when T_a is 20 °C, while the impact of the maximum error (3 m/s) on V_s will only lead to a deviation of 0.8 °C in UTCI when T_a is 35 °C. This sensitivity analysis implies that the uncertainty in the interpolated V_s propagating into the UTCI can be ignored during heat wave periods ($T_a > 35$ °C). Nevertheless, to suppress the impact of V_s, the Weather Research and Forecasting (WRF) model, rather than simple interpolation, can be used to assist in mapping UTCI over urban agglomeration.

4.3.3. Future prospects

Although progress has been made in UTCI mapping on the basis of remote sensing, this study has several limitations. The spatial resolution of the UTCI maps remains low (1 km), and we only conducted the mapping under clear sky conditions considering the

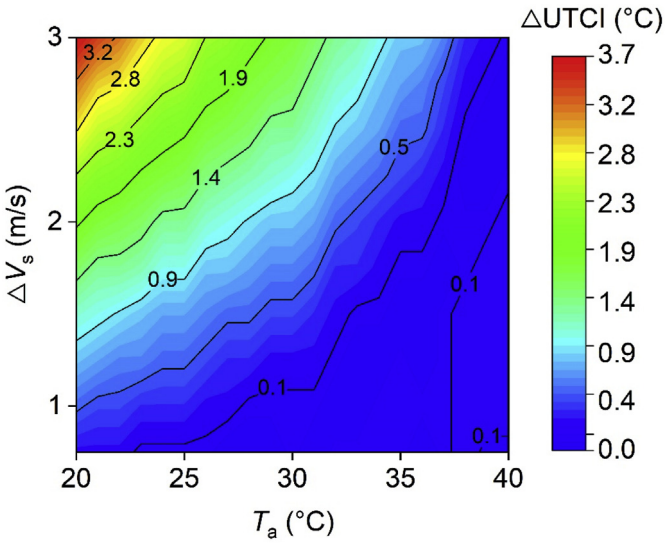

Fig. 13. Results of sensitivity analysis of the error in wind speed (V_s) for the estimation of UTCI with different ambient surface air temperature (T_a).

availability of remotely sensed T_s. In addition, the impact of urban geometry has not been fully considered. To improve the spatial resolution of the UTCI mapping, downscaling methods that are capable of disaggregating a coarse pixel into subpixels should be useful (Agam et al., 2007; Hutengs and Vohland, 2016; Xu et al., 2017; Zhan et al., 2013). To obtain the UTCI under all-weather conditions, T_s and its related parameters under cloudy conditions should be reconstructed before being used for mapping, by using the reconstruction methods of under-cloud T_s developed by the remote sensing community (Duan et al., 2017; Yu et al., 2014). In order to better understand the importance of urban geometry, especially over dense built-up areas, the combination of remote sensing data with computational fluid dynamics models (e.g., the ENVI-met model) may be viable (Battista et al., 2016; Park et al., 2014). Finally, during heat wave periods, the integration of the UTCI maps with socioeconomic, heat exposure, and disease data can lead to a better evaluation of health risks that is likely to improve the extreme weather warning systems and benefit urban planning (Chen et al., 2018; Hu et al., 2019; McGregor et al., 2015).

5. Conclusions

There is an absence of city-scale UTCI mapping over urban agglomerations and the relationship between the UTCI-based UHII and those based on other types of temperature is unclear. Consequently, we conducted UTCI mapping across the YRDUA based mainly on satellite data, and further compared the UHI intensities calculated with different temperatures (including the UTCI). Our major findings are summarized as follows.

First, during heat wave periods, the UTCI varies significantly among different land cover types – with the highest values mostly occurring within or around the cities. The daytime UTCI is spatially heterogeneous, while the nighttime UTCI is relatively uniform. The UTCI has the strongest correlation with the air temperature, among all the various types of temperature; however, the difference between the UTCI and the air temperature may be large over urban areas, with a maximum difference of 8.6 °C during the day.

Second, the thermal stress quantified by the UTCI has increased greatly with the rapid urbanization across the YRDUA during the past two decades. The area affected by 'very strong' thermal stress during the day expanded by 18.2% from 2002 to 2018, with the areas with prominent expansion mainly occurring around or within cities. Compared with the daytime case, nighttime heat stress increased more rapidly, with the area affected by 'strong' thermal stress accounting for the largest proportion (52.7%).

Third, the UHII related results show that the UTCI-based UHII is lower than those based on the LST (T_s) and mean radiant temperature (T_{mrt}), but greater than those based on surface air temperature (T_a) and dew-point temperature (T_d). Over Nanjing and Shanghai, the order of UHIIs based on different temperatures at night is consistent with that during the day. However, a different phenomenon occurs in Hangzhou, with the UTCI-based UHII (i.e., 0.96 °C) significantly higher than those based on the other types of temperature, probably due to the 'wall effect' created by the mountains surrounding Hangzhou.

We consider that our findings can facilitate the rapid city-scale assessment of thermal comfort across urban agglomeration during heat wave periods. The UTCI maps should also be valuable for related studies such as heat-related health risk assessment and regional planning.

CRediT authorship contribution statement

Chenguang Wang: Conceptualization, Methodology, Software, Formal analysis, Writing - original draft, Writing - review & editing. **Wenfeng Zhan:** Conceptualization, Methodology, Writing - review & editing, Supervision, Project administration, Funding acquisition. **Zihan Liu:** Writing - review & editing. **Jiufeng Li:** Writing - review & editing. **Long Li:** Writing - review & editing. **Peng Fu:** Writing - review & editing. **Fan Huang:** Writing - review & editing. **Jiameng Lai:** Writing - review & editing. **Jike Chen:** Writing - review & editing. **Falu Hong:** Writing - review & editing. **Sida Jiang:** Writing - review & editing.

Declaration of competing interest

The authors declare that they have no known competing financial interests or personal relationships that could have appeared to influence the work reported in this paper.

Acknowledgements

We are grateful to NASA's Land Processes Distributed Active Archive Center (LP DAAC) and the Weather Underground website (https://www.wunderground.com/) for providing the MODIS products and meteorological data, respectively. This work was supported in part by the National Key R&D Program of China under Grant number 2017YFA0603604, the National Natural Science Foundation of China under Grant number 41671420, the Jiangsu Provincial Natural Science Foundation under Grand number BK20180009, the Fundamental Research Funds for the Central Universities under Grant number 090414380024, and the Ministry Science and Technology Development of China-Data Sharing Infrastructure of Earth System Science under 2005DKA32300. We are also grateful for the financial support provided by the National Youth Talent Support Program of China.

Appendix A. Validation of retrieved T_a and T_d

The generated surface air temperatures (T_a) and dew-point temperatures (T_d) were compared with *in-situ* observations. The validation shown in Fig. A1 demonstrates that the RMSE and bias for T_a are 1.79 and 0.49 °C, respectively, while those for T_d are 2.39 and −0.43 °C, respectively. The accuracy of T_d is lower than for T_a, due mainly to the greater difficulty in estimating near-surface humidity with satellite data (Zhang et al., 2014).

This degree of accuracy is acceptable, especially considering the difference in spatial scale between the satellite-derived (with a spatial resolution of 5 km) and *in-situ* measurements, as well as the difference in temporal sampling. The satellite-derived measurements are instantaneous, while the *in-situ* measurements were collected every half-hour (Zhu et al., 2017). This level of accuracy is also satisfactory when compared with that in terms of the estimation of T_a and T_d by remote sensing (Benali et al., 2012; Bisht and Bras, 2010; Famiglietti et al., 2018; Zakšek and Schroedter-Homscheidt, 2009).

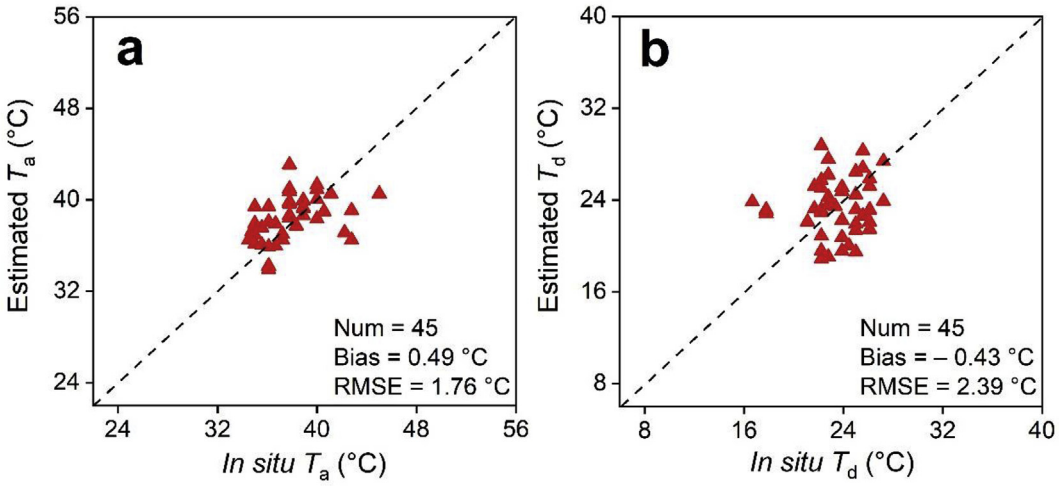

Fig. A1. Validation of estimated surface air temperature (T_a) (**a**) and dew-point temperature (T_d) (**b**) versus measured values.

References

Agam, N., Kustas, W.P., Anderson, M.C., Li, F., Neale, C.M., 2007. A vegetation index based technique for spatial sharpening of thermal imagery. Remote Sens. Environ. 107 (4), 545–558. https://doi.org/10.1016/j.rse.2006.10.006.

Alavipanah, S., Schreyer, J., Haase, D., Lakes, T., Qureshi, S., 2018. The effect of multi-dimensional indicators on urban thermal conditions. J. Clean. Prod. 177, 115–123. https://doi.org/10.1016/j.jclepro.2017.12.187.

Anderson, B.G., Bell, M.L., 2009. Weather-related mortality: how heat, cold, and heat waves affect mortality in the United States. Epidemiology (Cambridge, Mass.) 20 (2), 205. https://doi.org/10.1097/EDE.0b013e318190ee08.

Anderson, G.B., Bell, M.L., 2010. Heat waves in the United States: mortality risk during heat waves and effect modification by heat wave characteristics in 43 US communities. Environ. Health Perspect. 119 (2), 210–218. https://doi.org/10.1289/ehp.1002313.

Apaydin, H., Sonmez, F.K., Yildirim, Y.E., 2004. Spatial interpolation techniques for climate data in the GAP region in Turkey. Clim. Res. 28 (1), 31–40. https://doi.org/10.3354/cr028031.

Arghavani, S., Malakooti, H., Ali Akbari Bidokhti, A.-A., 2020. Numerical assessment of the urban green space scenarios on urban heat island and thermal comfort level in Tehran Metropolis. J. Clean. Prod. 121183 https://doi.org/10.1016/j.jclepro.2020.121183.

Barriopedro, D., Fischer, E.M., Luterbacher, J., Trigo, R.M., García-Herrera, R., 2011. The hot summer of 2010: redrawing the temperature record map of Europe. Science 332 (6026), 220–224. https://doi.org/10.1126/science.1201224.

Battista, G., Carnielo, E., Vollaro, R.D.L., 2016. Thermal impact of a redeveloped area on localized urban microclimate: a case study in Rome. Energy Build. 133, 446–454. https://doi.org/10.1016/j.enbuild.2016.10.004.

Bechtel, B., 2015. A new global climatology of annual land surface temperature. Rem. Sens. 7 (3), 2850–2870. https://doi.org/10.3390/rs70302850.

Benali, A., Carvalho, A.C., Nunes, J.P., Carvalhais, N., Santos, A., 2012. Estimating air surface temperature in Portugal using MODIS LST data. Remote Sens. Environ. 124, 108–121. https://doi.org/10.1016/j.rse.2012.04.024.

Bisht, G., Bras, R.L., 2010. Estimation of net radiation from the MODIS data under all sky conditions: southern Great Plains case study. Remote Sens. Environ. 114 (7), 1522–1534. https://doi.org/10.1016/j.rse.2010.02.007.

Błażejczyk, K., 2001. Assessment of recreational potential of bioclimate based on the human heat balance. In First International Workshop on Climate Tourism and Recreation. Int. J. Biometeorol. 133–152.

Błażejczyk, K., 2007. Multiannual and seasonal weather fluctuations and tourism in Poland. Climate change and tourism assessment and copying strategies. Maastricht-Warsaw-Freiburg 69–90.

Błażejczyk, K., Matzarakis, A., 2007. Assessment of bioclimatic differentiation of Poland based on the human heat balance. Geogr. Pol. 80 (1), 63–82.

Błażejczyk, K., 2011. Mapping of UTCI in local scale (the case of Warsaw). Prace i Studia Geograficzne WGSR UW 47, 275–283.

Błażejczyk, K., Epstein, Y., Jendritzky, G., Staiger, H., Tinz, B., 2012. Comparison of UTCI to selected thermal indices. Int. J. Biometeorol. 56 (3), 515–535. https://doi.org/10.1007/s00484-011-0453-2.

Błażejczyk, K., Jendritzky, G., Bröde, P., Fiala, D., Havenith, G., Epstein, Y., Psikuta, A., Kampmann, B., 2013. An introduction to the universal thermal climate index (UTCI). Geogr. Pol. 86 (1), 5–10. https://doi.org/10.7163/GPol.2013.1.

Błażejczyk, K., Kuchcik, M., Błażejczyk, A., Milewski, P., Szmyd, J., 2014. Assessment of urban thermal stress by UTCI–experimental and modelling studies: an example from Poland. DIE ERDE. J. Geogr. Soc. Berl. 145 (1–2), 16–33. https://doi.org/10.12854/erde-145-3.

Bröde, P., Krüger, E.L., Rossi, F.A., Fiala, D., 2012a. Predicting urban outdoor thermal comfort by the Universal Thermal Climate Index UTCI–a case study in Southern Brazil. Int. J. Biometeorol. 56 (3), 471–480. https://doi.org/10.1007/s00484-011-0452-3.

Bröde, P., Fiala, D., Błażejczyk, K., Holmér, I., Jendritzky, G., Kampmann, B., Tinz, B., Havenith, G., 2012b. Deriving the operational procedure for the universal thermal climate index (UTCI). Int. J. Biometeorol. 56 (3), 481–494. https://doi.org/10.1007/s00484-011-0454-1.

Bolton, D., 1980. The computation of equivalent potential temperature. Mon. Weather Rev. 108 (7), 1046–1053. https://doi.org/10.1175/1520-0493(1980)108<1046:TCOEPT>2.0.CO;2.

Chen, L., Ng, E., 2011. Quantitative urban climate mapping based on a geographical database: a simulation approach using Hong Kong as a case study. Int. J. Appl. Earth Obs. Geoinf. 13 (4), 586–594. https://doi.org/10.1016/j.jag.2011.03.003.

Chen, Y.C., Chen, C.Y., Matzarakis, A., Liu, J.K., Lin, T.P., 2016. Modeling of mean radiant temperature based on comparison of airborne remote sensing data with surface measured data. Atmos. Res. 174, 151–159. https://doi.org/10.1016/j.atmosres.2016.01.004.

Chen, Q., Ding, M., Yang, X., Hu, K., Qi, J., 2018. Spatially explicit assessment of heat health risk by using multi-sensor remote sensing images and socioeconomic data in Yangtze River Delta, China. Int. J. Health Geogr. 17 (1), 15. https://doi.org/10.1186/s12942-018-0135-y.

Clark, R.P., Edholm, O.G., 1985. Man and His Thermal Environment. Arnold, London. https://doi.org/10.1016/0003-6870(86)90056-6.

Clinton, N., Gong, P., 2013. MODIS detected surface urban heat islands and sinks: global locations and controls. Remote Sens. Environ. 134, 294–304. https://doi.org/10.1016/j.rse.2013.03.008.

Di Napoli, C., Pappenberger, F., Cloke, H.L., 2018. Assessing heat-related health risk in europe via the universal thermal climate index (UTCI). Int. J. Biometeorol. 62 (7), 1155–1165. https://doi.org/10.1007/s00484-018-1518-2.

Duan, S.B., Li, Z.L., Leng, P., 2017. A framework for the retrieval of all-weather land surface temperature at a high spatial resolution from polar-orbiting thermal infrared and passive microwave data. Remote Sens. Environ. 195, 107–117. https://doi.org/10.1016/j.rse.2017.04.008.

ECMWF, 2020. The ERA5-HEAT dataset product user guide. http://datastore.copernicus-climate.eu/c3s/published-forms/c3sprod/derived-utci-historical/UTCIMRTdatabase_UserGuide.pdf.
Famiglietti, C.A., Fisher, J.B., Halverson, G., Borbas, E.E., 2018. Global validation of MODIS near-surface air and dew point temperatures. Geophys. Res. Lett. 45 (15), 7772–7780. https://doi.org/10.1029/2018GL077813.
Fanger, P.O., 1970. Thermal Comfort Analysis and Applications in Environmental Engineering. McGraw Hill, New York.
Feng, J.M., Wang, Y.L., Ma, Z.G., Liu, Y.H., 2012. Simulating the regional impacts of urbanization and anthropogenic heat release on climate across China. J. Clim. 25 (20), 7187–7203. https://doi.org/10.1175/jcli-d-11-00333.1.
Fiala, D., Havenith, G., Bröde, P., Kampmann, B., Jendritzky, G., 2012. UTCI-Fiala multi-node model of human heat transfer and temperature regulation. Int. J. Biometeorol. 56 (3), 429–441. https://doi.org/10.1007/s00484-011-0424-7.
Gagge, A.P., Fobelets, A.P., Berglund, L., 1986. A standard predictive Index of human reponse to thermal enviroment. Transactions/American Society of Heating, Refrigerating and Air-Conditioning Engineers 92 (2B), 709–731.
Gao, J., Sun, Y., Liu, Q., Zhou, M., Lu, Y., Li, L., 2015. Impact of extreme high temperature on mortality and regional level definition of heat wave: a multi-city study in China. Sci. Total Environ. 505, 535–544. https://doi.org/10.1016/j.scitotenv.2014.10.028.
Ge, Q., Kong, Q., Xi, J., Zheng, J., 2017. Application of UTCI in China from tourism perspective. Theor. Appl. Climatol. 128 (3–4), 551–561. https://doi.org/10.1007/s00704-016-1731-z.
Gonzalez, R.R., Nishi, Y., Gagge, A.P., 1974. Experimental evaluation of standard effective temperature a new biometeorological index of man's thermal discomfort. Int. J. Biometeorol. 18 (1), 1–15. https://doi.org/10.1007/BF01450660.
Hajat, S., O'Connor, M., Kosatsky, T., 2010. Health effects of hot weather: from awareness of risk factors to effective health protection. Lancet 375 (9717), 856–863. https://doi.org/10.1016/S0140-6736(09)61711-6.
Höppe, P., 2002. Different aspects of assessing indoor and outdoor thermal comfort. Energy Build. 34 (6), 661–665. https://doi.org/10.1016/S0378-7788(02)00017-8.
He, X., Wang, J., Feng, J., Yan, Z., Miao, S., Zhang, Y., Xia, J., 2020. Observational and modeling study of interactions between urban heat island and heatwave in Beijing. J. Clean. Prod. 247 https://doi.org/10.1016/j.jclepro.2019.119169, 119169.
Ho, H.C., Knudby, A., Sirovyak, P., Xu, Y., Hodul, M., Henderson, S.B., 2014. Mapping maximum urban air temperature on hot summer days. Remote Sens. Environ. 154, 38–45. https://doi.org/10.1016/j.rse.2014.08.012.
Ho, H.C., Knudby, A., Xu, Y., Hodul, M., Aminipouri, M., 2016. A comparison of urban heat islands mapped using skin temperature, air temperature, and apparent temperature (Humidex), for the greater Vancouver area. Sci. Total Environ. 544, 929–938. https://doi.org/10.1016/j.scitotenv.2015.12.021.
Huang, W., Kan, H., Kovats, S., 2010. The impact of the 2003 heat wave on mortality in Shanghai, China. Sci. Total Environ. 408 (11), 2418–2420. https://doi.org/10.1016/j.scitotenv.2010.02.009.
Hu, L., Brunsell, N.A., 2015. A new perspective to assess the urban heat island through remotely sensed atmospheric profiles. Remote Sens. Environ. 158, 393–406. https://doi.org/10.1016/j.rse.2014.10.022.
Hu, K., Yang, X., Zhong, J., Fei, F., Qi, J., 2017. Spatially explicit mapping of heat health risk utilizing environmental and socioeconomic data. Environ. Sci. Technol. 51 (3), 1498–1507. https://doi.org/10.1021/acs.est.6b04355.
Hu, K., Guo, Y., Yang, X., Zhong, J., Fei, F., Chen, F., Zhao, Q., Zhang, Y., Chen, G., Chen, Q., Ye, T., Li, S., Qi, J., 2019. Temperature variability and mortality in rural and urban areas in Zhejiang province, China: an application of a spatiotemporal index. Sci. Total Environ. 647, 1044–1051. https://doi.org/10.1016/j.scitotenv.2018.08.095.
Hutengs, C., Vohland, M., 2016. Downscaling land surface temperatures at regional scales with random forest regression. Remote Sens. Environ. 178, 127–141. https://doi.org/10.1016/j.rse.2016.03.006.
Imhoff, M.L., Zhang, P., Wolfe, R.E., Bounoua, L., 2010. Remote sensing of the urban heat island effect across biomes in the continental USA. Remote Sens. Environ. 114 (3), 504–513. https://doi.org/10.1016/j.rse.2009.10.008.
Imran, H.M., Kala, J., Ng, A.W.M., Muthukumaran, S., 2018. Effectiveness of green and cool roofs in mitigating urban heat island effects during a heatwave event in the city of Melbourne in southeast Australia. J. Clean. Prod. 197, 393–405. https://doi.org/10.1016/j.jclepro.2018.06.179.
Jang, K., Kang, S., Kim, J., Lee, C.B., Kim, T., Kim, J., Hirata, R., Saigusa, N., 2010. Mapping evapotranspiration using MODIS and MM5 four-dimensional data assimilation. Remote Sens. Environ. 114 (3), 657–673. https://doi.org/10.1016/j.rse.2009.11.010.
Jendritzky, G., Tinz, B., 2009. The thermal environment of the human being on the global scale. Glob. Health Action 2 (1). https://doi.org/10.3402/gha.v2i0.2005, 2005.
Jendritzky, G., de Dear, R., Havenith, G., 2012. UTCI–why another thermal index? Int. J. Biometeorol. 56 (3), 421–428. https://doi.org/10.1007/s00484-011-0513-7.
Johansson, E., Emmanuel, R., 2006. The influence of urban design on outdoor thermal comfort in the hot, humid city of Colombo, Sri Lanka. Int. J. Biometeorol. 51 (2), 119–133. https://doi.org/10.1007/s00484-006-0047-6.
Kenny, N.A., Warland, J.S., Brown, R.D., Gillespie, T.G., 2008. Estimating the radiation absorbed by a human. Int. J. Biometeorol. 52 (6), 491–503. https://doi.org/10.1007/s00484-008-0145-8.
Kong, Q., Ge, Q., Xi, J., Zheng, J., 2017. Human-biometeorological assessment of increasing summertime extreme heat events in Shanghai, China during 1973-2015. Theor. Appl. Climatol. 130 (3–4), 1055–1064. https://doi.org/10.1007/s00704-016-1933-4.
Lai, D., Liu, W., Gan, T., Liu, K., Chen, Q., 2019. A review of mitigating strategies to improve the thermal environment and thermal comfort in urban outdoor spaces. Sci. Total Environ. 661, 337–353. https://doi.org/10.1016/j.scitotenv.2019.01.062.
Lavell, A., Oppenheimer, M., Diop, C., Hess, J., Lempert, R., Li, J., Muir-Wood, R., Myeong, S., Moser, S., Takeuchi, K., Cardona, O.D., Hallegatte, S., Lemos, M., Little, C., Lotsch, A., Weber, Elke U., 2012. Climate change: new dimensions in disaster risk, exposure, vulnerability, and resilience. In: Managing the Risks of Extreme Events and Disasters to Advance Climate Change Adaptation: Special Report of the Intergovernmental Panel on Climate Change. Cambridge University Press, pp. 25–64. https://doi.org/10.1007/s11783-011-0280-z.
Li, D., Bou-Zeid, E., 2013. Synergistic interactions between urban heat islands and heat waves: the impact in cities is larger than the sum of its parts. J. Appl. Meteorol. Climatol. 52 (9), 2051–2064. https://doi.org/10.1175/JAMC-D-13-02.1.
Li, Z.L., Tang, B.H., Wu, H., Ren, H., Yan, G., Wan, Z., Trigo, I.F., Sobrino, J.A., 2013. Satellite-derived land surface temperature: current status and perspectives. Remote Sens. Environ. 131, 14–37. https://doi.org/10.1016/j.rse.2012.12.008.
Liu, K., Li, X., Wang, S., Li, Y., 2020a. Investigating the impacts of driving factors on urban heat islands in southern China from 2003 to 2015. J. Clean. Prod. 254 https://doi.org/10.1016/j.jclepro.2020.120141, 120141.
Liu, X., Zhou, Y., Yue, W., Li, X., Liu, Y., Lu, D., 2020b. Spatiotemporal patterns of summer urban heat island in Beijing, China using an improved land surface temperature. J. Clean. Prod. 257 https://doi.org/10.1016/j.jclepro.2020.120529, 120529.
Lokys, H.L., Junk, J., Krein, A., 2018. Short-term effects of air quality and thermal stress on non-accidental morbidity—a multivariate meta-analysis comparing indices to single measures. Int. J. Biometeorol. 62 (1), 17–27. https://doi.org/10.1007/s00484-017-1326-0.
Luo, W., Taylor, M.C., Parker, S.R., 2008. A comparison of spatial interpolation methods to estimate continuous wind speed surfaces using irregularly distributed data from England and Wales. Int. J. Climatol.: J. R. Meteorol. Soc 28 (7), 947–959. https://doi.org/10.1002/joc.1583.
Matzarakis, A., Rutz, F., Mayer, H., 2010. Modelling radiation fluxes in simple and complex environments: basics of the RayMan model. Int. J. Biometeorol. 54 (2), 131–139. https://doi.org/10.1007/s00484-009-0261-0.
Mayer, H., Höppe, P., 1987. Thermal comfort of man in different urban environments. Theor. Appl. Climatol. 38 (1), 43–49. https://doi.org/10.1007/bf00866252.
McGregor, G.R., Bessmoulin, P., Ebi, K., Menne, B., 2015. Heatwaves and Health: Guidance on Warning-System Development. World Meteorological Organization and World Health Organization. http://www.who.int/globalchange/publications/heatwaves-health-guidance/en/.
Meehl, G.A., Tebaldi, C., 2004. More intense, more frequent, and longer lasting heat waves in the 21st century. Science 305 (5686), 994–997. https://doi.org/10.1126/science.1098704.
Mijorski, S., Cammelli, S., Green, J., 2019. A hybrid approach for the assessment of outdoor thermal comfort. J. Build Eng. 22, 147–153. https://doi.org/10.1016/j.jobe.2018.12.003.
Mora, C., Dousset, B., Caldwell, I.R., Powell, F.E., Geronimo1, R.C., Bielecki, C.R., Counsell, C.W.W., Dietrich, B.S., Johnston, E.T., Louis, L.V., Lucas, M.P., McKenzie1, M.M., Shea1, A.G., Tseng, H., Giambelluca, T.W., Leon, L.R., Hawkins, E., Trauernicht, C., 2017. Global risk of deadly heat. Nat. Clim. Change 7 (7), 501. https://doi.org/10.1038/nclimate3322.
Nastos, P.T., Matzarakis, A., 2012. The effect of air temperature and human thermal indices on mortality in Athens, Greece. Theor. Appl. Climatol. 108 (3–4), 591–599. https://doi.org/10.1007/s00704-011-0555-0.
Oke, T.R., Mills, G., Christen, A., Voogt, J.A., 2017. Urban Climates. Cambridge University Press.
Pantavou, K., Theoharatos, G., Santamouris, M., Asimakopoulos, D., 2013. Outdoor thermal sensation of pedestrians in a Mediterranean climate and a comparison with UTCI. Build. Environ. 66, 82–95. https://doi.org/10.1016/j.buildenv.2013.02.014.
Pappenberger, F., Jendritzky, G., Staiger, H., Dutra, E., Di Giuseppe, F., Richardson, D.S., Cloke, H.L., 2015. Global forecasting of thermal health hazards: the skill of probabilistic predictions of the Universal Thermal Climate Index (UTCI). Int. J. Biometeorol. 59 (3), 311–323. https://doi.org/10.1007/s00484-014-0843-3.
Park, S., Tuller, S.E., 2011. Comparison of human radiation exchange models in outdoor areas. Theor. Appl. Climatol. 105 (3–4), 357–370. https://doi.org/10.1007/s00704-010-0388-2.
Park, S., Tuller, S.E., Jo, M., 2014. Application of Universal Thermal Climate Index (UTCI) for microclimatic analysis in urban thermal environments. Landsc. Urban Plann. 125, 146–155. https://doi.org/10.1016/j.landurbplan.2014.02.014.
Potchter, O., Cohen, P., Lin, T.P., Matzarakis, A., 2018. Outdoor human thermal perception in various climates: a comprehensive review of approaches, methods and quantification. Sci. Total Environ. 631, 390–406. https://doi.org/10.1016/j.scitotenv.2018.02.276.
Prihodko, L., Goward, S.N., 1997. Estimation of air temperature from remotely sensed surface observations. Remote Sens. Environ. 60 (3), 335–346. https://doi.org/10.1016/s0034-4257(96)00216-7.
Psikuta, A., Fiala, D., Laschewski, G., Jendritzky, G., Richards, M., Błażejczyk, K., Havenith, G., Mekjavič, I., Rintamäki, H., de Dear, R., George, Havenit, 2012. Validation of the Fiala multi-node thermophysiological model for UTCI application. Int. J. Biometeorol. 56 (3), 443–460. https://doi.org/10.1007/s00484-

011-0450-5.
Roshan, G., Almomenin, H.S., da Silveira Hirashima, S.Q., Attia, S., 2019. Estimate of outdoor thermal comfort zones for different climatic regions of Iran. Urban Clim 27, 8–23. https://doi.org/10.1016/j.uclim.2018.10.005.
Schwartz, J., Samet, J.M., Patz, J.A., 2004. Hospital admissions for heart disease: the effects of temperature and humidity. Epidemiology 15 (6), 755–761. https://doi.org/10.2307/20485985.
Staiger, H., Laschewski, G., Grätz, A., 2012. The perceived temperature—a versatile index for the assessment of the human thermal environment. Part A: scientific basics. Int. J. Biometeorol. 56 (1), 165–176. https://doi.org/10.1007/s00484-011-0409-6.
Sun, X., Sun, Q., Zhou, X., Li, X., Yang, M., Yu, A., Geng, F., 2014. Heat wave impact on mortality in pudong new area, China in 2013. Sci. Total Environ. 493, 789–794. https://doi.org/10.1016/j.scitotenv.2014.06.042.
Thorsson, S., Rocklöv, J., Konarska, J., Lindberg, F., Holmer, B., Dousset, B., Rayner, D., 2014. Mean radiant temperature—A predictor of heat related mortality. Urban Clim 10, 332–345. https://doi.org/10.1016/j.uclim.2014.01.004.
Trenberth, K.E., Fasullo, J.T., 2012. Climate extremes and climate change: the Russian heat wave and other climate extremes of 2010. J. Geophys. Res. Atmos. 117 (D17) https://doi.org/10.1029/2012JD018020.
Tumini, I., Higueras García, E., Baereswyl Rada, S., 2016. Urban microclimate and thermal comfort modelling: strategies for urban renovation. Int. J. Sustain. Build Tech. Urban Dev. 7 (1), 22–37. https://doi.org/10.1080/2093761X.2016.1152204.
Voogt, J.A., Oke, T.R., 2003. Thermal remote sensing of urban climates. Remote Sens. Environ. 86 (3), 370–384. https://doi.org/10.1016/s0034-4257(03)00079-8.
Winslow, C.E., Herrington, L.P., Gagge, A.P., 1936. A new method of partitional calorimetry. Am. J. Phys-Leg. Content. 116 (3), 641–655.
Wong, M., Nichol, J., Ng, E., 2011. A study of the "wall effect" caused by proliferation of high-rise buildings using GIS techniques. Landsc. Urban Plann. 102, 245–253. https://doi.org/10.1016/j.landurbplan.2011.05.003.
Xu, Y., Knudby, A., Ho, H.C., 2014. Estimating daily maximum air temperature from MODIS in British Columbia, Canada. Int. J. Rem. Sens. 35 (24), 8108–8121. https://doi.org/10.1080/01431161.2014.978957.
Xu, H., Hu, X., Guan, H., He, G., 2017. Development of a fine-scale discomfort index map and its application in measuring living environments using remotely-sensed thermal infrared imagery. Energy Build. 150, 598–607. https://doi.org/10.1016/j.enbuild.2017.06.003.
Xu, X., Wu, Y., Wang, W., Hong, T., Xu, N., 2019. Performance-driven optimization of urban open space configuration in the cold-winter and hot-summer region of China. Build. Simul. 12 (3), 411–424. https://doi.org/10.1007/s12273-019-0510-z.
Yang, X., Ruby Leung, L., Zhao, N., Zhao, C., Qian, Y., Hu, K., Liu, X., Chen, B., 2017. Contribution of urbanization to the increase of extreme heat events in an urban agglomeration in east China. Geophys. Res. Lett. 44 (13), 6940–6950. https://doi.org/10.1002/2017GL074084.
Yang, J., Zhang, Z., Li, X., Xi, J., Feng, Z., 2018. Spatial differentiation of China's summer tourist destinations based on climatic suitability using the Universal Thermal Climate Index. Theor. Appl. Climatol. 134 (3–4), 859–874. https://doi.org/10.1007/s00704-017-2312-5.
Yu, W., Ma, M., Wang, X., Tan, J., 2014. Estimating the land-surface temperature of pixels covered by clouds in MODIS products. J. Appl. Remote Sens. 8 (1), 083525 https://doi.org/10.1117/1.JRS.8.083525.
Zakšek, K., Schroedter-Homscheidt, M., 2009. Parameterization of air temperature in high temporal and spatial resolution from a combination of the SEVIRI and MODIS instruments. ISPRS-J. Photogramm. Remote Sens. 64 (4), 414–421. https://doi.org/10.1016/j.isprsjprs.2009.02.006.
Zhan, W., Chen, Y., Zhou, J., Wang, J., Liu, W., Voogt, J., Zhu, X., Quan, J., Li, J., 2013. Disaggregation of remotely sensed land surface temperature: literature survey, taxonomy, issues, and caveats. Remote Sens. Environ. 131, 119–139. https://doi.org/10.1016/j.rse.2012.12.014.
Zhang, H., Wu, B., Yan, N., Zhu, W., Feng, X., 2014. An improved satellite-based approach for estimating vapor pressure deficit from MODIS data. J. Geophys. Res. Atmos. 119 (21), 12–256. https://doi.org/10.1002/2014JD022118.
Zhu, W., Lű, A., Jia, S., Yan, J., Mahmood, R., 2017. Retrievals of all-weather daytime air temperature from MODIS products. Remote Sens. Environ. 189, 152–163. https://doi.org/10.1016/j.rse.2016.11.011.
Zuo, J., Pullen, S., Palmer, J., Bennetts, H., Chileshe, N., Ma, T., 2015. Impacts of heat waves and corresponding measures: a review. J. Clean. Prod. 92, 1–12. https://doi.org/10.1016/j.jclepro.2014.12.078.